JOURNAL OF MATERIALS SCIENCE 29 (1994) 1265–1275

Densification studies of SRBSN with unstabilized zirconia by means of dilatometry and electron microscopy

H.-J. KLEEBE (1), W. BRAUE (2), W. LUXEM (2)
(1) Max-Planck-Institut für Metallforschung, Institut für Werkstoffwissenschaft, D-70174 Stuttgart 1, Germany and (2) Deutsche Forschungsanstalt für Luft- und Raumfahrt, (DLR) Institut für Werkstoff-Forschung, D-51140 Köln, Germany*

A correlation of densification behaviour and microstructural development of ZrO_2-fluxed sintered reaction-bonded Si_3N_4 (SRBSN) is reported in the light of dilatometry and both high-resolution electron microscopy (HREM) and analytical electron microscopy (AEM). Two distinct dilatometer maxima were observed using a modified dilatometer with improved sensitivity. The relatively small first dilatometer maximum, at approximately 1750 °C, is due to the formation of a highly viscous silica-rich liquid phase at the initial stage of sintering. The second maximum, showing a more pronounced densification rate, is related to a radical change in secondary-phase chemistry at approximately 1900 °C. In the SRBSN system, ZrO_2 acts as an effective sintering aid because of the increased sintering temperatures and high N_2 overpressure during the second dilatometer event, which promotes active participation of ZrO_2 in the liquid-phase formation process. Sintering cycles were interrupted at the temperatures corresponding to the two dilatometer maxima. From these specimens, thin TEM foils were prepared, which correspond to the microstructures of the two densification events. Conventional TEM and HREM observations revealed significant microstructural differences, which could be related to the densification behaviour of the SRBSN–ZrO_2 system. The good high-temperature performance of the densified SRBSN material is due to (i) the formation of *in situ* large-grown β-Si_3N_4 grains, (ii) a completely crystallized secondary phase (m-ZrO_2), and (iii) very thin amorphous phase- and grain-boundary films of approximately 1.0 and 0.5 nm, respectively.

1. Introduction

Silicon nitride cannot be fully densified by classical solid-state sintering mechanisms, due to its high covalent bonding character and low self-diffusivity. Therefore, the addition of sintering aids is a prerequisite to promote liquid-phase sintering in order to achieve nearly complete densification [1–3]. During sintering, these additives react with silicon nitride and silica, which is always present on the Si_3N_4-particle surfaces, forming an eutectic liquid which promotes both particle rearrangement and solution–reprecipitation processes. Upon cooling the liquid phase formed at high temperatures is present as an amorphous phase at triple-grain junctions and along grain and phase boundaries. Large amounts of sintering additives result in well-known detrimental effects on high-temperature mechanical properties, e.g. creep behaviour and flexural strength, thus requiring a significant reduction in their volume fraction. In most systems, the amorphous phase present at three- and four-grain junctions can be partly crystallized via an additional heat-treatment procedure. Another approach to improve the high-temperature properties takes advantage of the refractoriness of rare-earth and certain transition element-based oxides, which increase the transition temperature of the liquid phase formed [4–6]. Following the latter approach, a small amount of unstabilized zirconia addition was utilized in this study. Although the Si_3N_4–ZrO_2 system has received considerable attention from numerous research groups, the majority of reports have focused on the effect of yttria-stabilized ZrO_2 on densification and microstructural development [7–12]. Nevertheless, evidence for the suitability of unstabilized ZrO_2 as a sintering aid for hot-pressed Si_3N_4 dates back to the early 1960s and 1970s [13, 14].

In order to achieve full densification with 5 wt % unstabilized ZrO_2 addition, the Si_3N_4 materials investigated were prepared via the reaction-bonded Si_3N_4 (RBSN) route with subsequent gas-pressure sintering [15]. Compared to pressureless sintered silicon nitride materials (SSN) of similar additive compositions, such gas-pressure sintered RBSN grades (SRBSN) are characterized by (i) lower shrinkage rates during densification, (ii) the possibility of markedly reducing the additive content, and (iii) utilizing more refractory sintering aids [16–18]. The main emphasis of this study is on the evaluation of the sintering

* *Now at:* Universität Bayréuth Institut für Material forschung D-95440 Bayréuth, Germany

0022–2461

behaviour in the SRBSN–ZrO_2 system. Because of the fact that (i) unstabilized zirconia was added to the powder blends prior to nitridation and subsequent sintering, and (ii) m-ZrO_2 still is observed as the prominent crystalline secondary phase after complete densification, the role of the zirconia addition in the overall sintering process required particular attention. Possible effects of the high-N_2 partial pressure on the stabilization of c-ZrO_2 and/or the formation of constituents in the system ZrO_2–ZrN during densification of SRBSN–ZrO_2 materials were also investigated. As this study is based on well-defined SRBSN microstructures, it focuses on the correlation of microstructural features, observed by means of high-resolution and analytical transmission electron microscopy, with distinct densification events, as monitored via dilatometry during gas-pressure sintering.

2. Experimental and instrumentation

The SRBSN material was processed via the RBSN route [19, 20]. Si-powder fluxed with unstabilized zirconia was nitrided at 0.1 MPa N_2-pressure and subsequently densified utilizing a two-step gas-pressure sintering cycle with increased N_2-pressure, as illustrated in the processing flow chart shown in Fig. 1.

Gas-pressure sintering usually follows four dT/dt ramps. The increase from room temperature to 1100 °C was achieved in approximately 1 h, followed by 20–30 min each for the 1100 to 1300 °C and the 1300 to 1875 °C intervals, respectively. To ensure the formation of closed porosity, the experiment was held for 20 min at this temperature (p_{N_2} = 1.5 MPa). Thereafter, the N_2-pressure was increased to a final 10 MPa with the temperature raised to 1925 °C and held for 60 min.

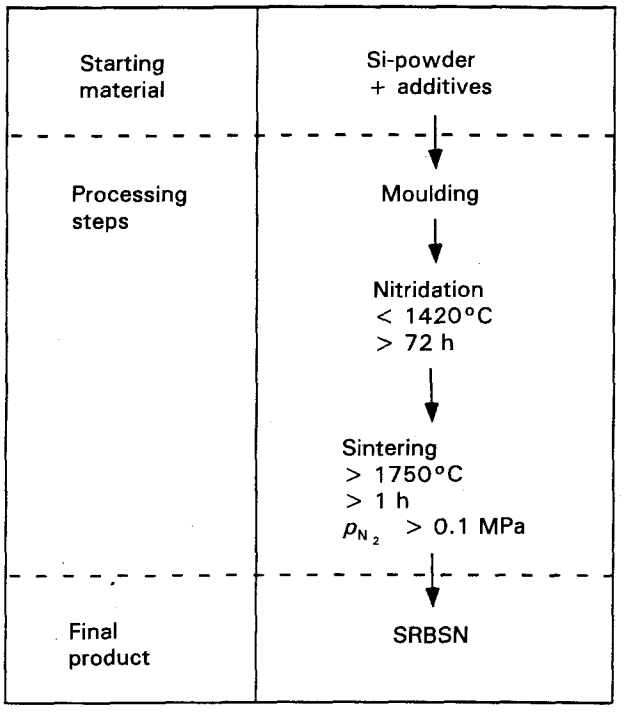

Figure 1 Flow chart of fabrication steps and typical processing conditions for the preparation of SRBSN materials.

During gas-pressure sintering a newly designed dilatometer [21] with improved control of the sintering atmosphere was attached to the specimen surface, which revealed two distinct densification events at 1730–1750 °C and 1900–1920 °C, depending on the heating rate of the experiment. The dilatometer measurements indicated densification rates unique to the zirconia fluxed system when compared with many other sintering additives. It is important to note that the densification rate during the first dilatometer maximum was very low with 0.5 μm min^{-1} compared to the second, which was strongly pronounced with 70 μm min^{-1} (see Fig. 2).

Qualitative phase analysis from bulk materials was determined by standard powder X-ray diffraction (XRD) techniques. The materials investigated revealed distinct differences in phase composition, as shown in Table 1.

Investigation of microstructures correlated with the dilatometer maxima was performed by conventional and high-resolution transmission electron microscopy utilizing a Philips EM 430 (300 kV) and a JEOL JEM 4000 EX operating at 400 kV (point-to-point resolution of 1.8 nm). Analytical electron microscopy involved small probe microanalysis (EDS, ELS) and convergent beam electron diffraction (CBED). Sintering cycles were interrupted at the very temperatures of the two dilatometer maxima. Electron-transparent TEM foils of materials corresponding to the densification events (see Fig. 2) were prepared by standard ceramographic techniques involving dimpling, ion beam thinning, and carbon coating to reduce electrostatic charging in the microscope.

3. Results and discussion

As the SRBSN–ZrO_2 material is characterized by two distinct densification events, this approach is organized into two sections focusing on the characteristic microstructure of each dilatometer maximum.

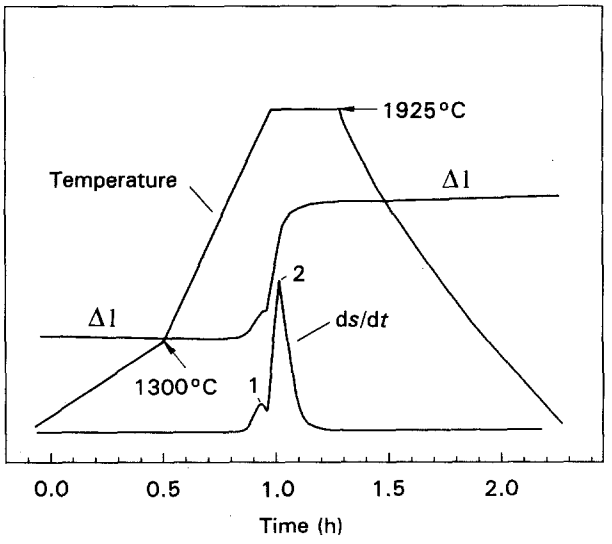

Figure 2 Dilatometer experiment of the SRBSN + 5 wt% ZrO_2 material in terms of the heating rate, shrinkage, and densification rate, respectively. The latter revealed two distinct densification events.

TABLE I SRBSN processing conditions (temperature, N_2-gas pressure), and corresponding phase content identified by means of X-ray diffraction for the first and second dilatometer maximum, respectively

	1st Dilatometer maximum	2nd Dilatometer maximum
Temperature (°C)	1730	1920
N_2-gas pressure (bars)	15	100
Phase content*	β-Si_3N_4	β-Si_3N_4
(X-ray data)	Si_2N_2O (α-Si_3N_4)	–
	m-ZrO_2	m-ZrO_2
	(traces of t-ZrO_2?)	(traces of t-ZrO_2?)

*no $ZrSiO_4$, ZrN or Zr-silicides were identified by X-ray and electron diffraction.

3.1. Microstructure of ZrO_2-fluxed SRBSN corresponding to the first dilatometer maximum

The specimen of the first dilatometer maximum showed distinct differences compared with the densified SRBSN material. The low-temperature sintered body consisted of homogeneously fine-grained β-Si_3N_4 particles with a relatively high amount of residual porosity of approximately 10 vol %, as estimated by TEM. As opposed to the fully dense material (see Section 3.2) no elongated large β-Si_3N_4 grains were present at this stage of microstructural development. However, some extended aggregates of the crystalline secondary phase (up to 5 μm), which are presumably due to agglomeration during powder processing, were occasionally observed (Fig. 3). It is important to note that these agglomerates are only present under the conditions of this low-temperature densification event and were not observed in the densified SRBSN grades. This indicates that the unstabilized zirconia addition does not contribute (or contributes a very limited amount) to the liquid-phase formation process as far as the first dilatometer event is concerned.

Apart from the very large agglomerates, with diameters up to several micrometres, crystalline Zr-bearing secondary phases are present at three- and four-grain junctions, which exhibit different grain morphologies: (i) irregularly shaped aggregates of m-ZrO_2, filling the space between Si_3N_4 and Si_2N_2O crystals, as shown in Fig. 4 a and b and (ii) relatively small, lath-shaped, heavily twinned crystals, which also were identified as m-ZrO_2 (compare Fig. 5 a–c). The internal structure of the m-ZrO_2 grains is characterized by different twinned sections and thus by mosaic-like structures, as previously described [22–24]. The lack of additional ZrO_2 polymorphs besides m-ZrO_2 in specimens from the first dilatometer maximum (see Table 1) is interesting, and merits some comments in terms of appropriate methods for qualitative phase analysis. X-ray diffraction the m-ZrO_2 polymorph can be distinguished from c-ZrO_2 and t-ZrO_2 by means of {1 1 1} reflections, while a separation of the latter polymorphs is possible through splitting of low-angle {2 0 0} and high-angle {4 0 0} reflections, respectively [25, 26]. Very weak X-ray signals, which could not unambiguously be attributed to c- and/or t-ZrO_2 symmetries, were observed for specimens from both dilatometer maxima (see Table 1). However, with respect to such fundamental issues as the possible stabilization of c-ZrO_2 and/or t-ZrO_2 in the SRBSN–ZrO_2 materials, the significance of these X-ray findings is regarded as inappropriate to furnish more than a rough characterization tool of the phase assemblages involved. For this reason, particular attention is directed to phase determination by means of high-resolution and analytical TEM techniques, including small-probe microanalysis and CBED. The lack of grains exhibiting other than monoclinic symmetry became evident during extensive tilting of the TEM foil and careful inspections of a large number of oriented crystals via HREM and electron diffraction, as described below. Moreover, the grain size of most Zr-bearing secondary phases is too large to account for a possible metastable retention of the tetragonal symmetry [22, 24]. These conclusions are not restricted to the SRBSN–ZrO_2 microstructure, which corresponds to the first dilatometer maximum; as discussed in Section 3.2, it is also true for the second densification event.

Although unstabilized zirconia was employed in this study, possible formation of nitride-stabilized c-ZrO_2 [31] and/or Zr-oxinitrides [27-33] was anticipated. In nitride-stabilized c-ZrO_2, partial substitution of nitrogen for oxygen in ZrO_2 through addition of AlN, Mg_3N_2, ZrN or Si_3N_4 is believed to create vacancies in the anion sublattice, similar to the effects of rare-earth oxides, thus stabilizing the cubic poly-

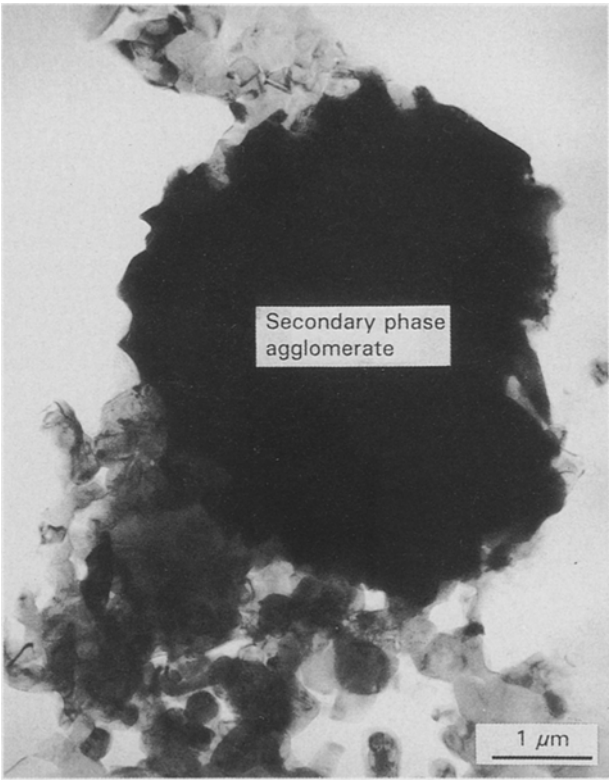

Figure 3 Low magnification TEM micrograph depicting a large secondary phase agglomerate of the crystalline secondary phase surrounded by a fine-grained Si_3N_4 matrix which shows residual porosity (first densification event).

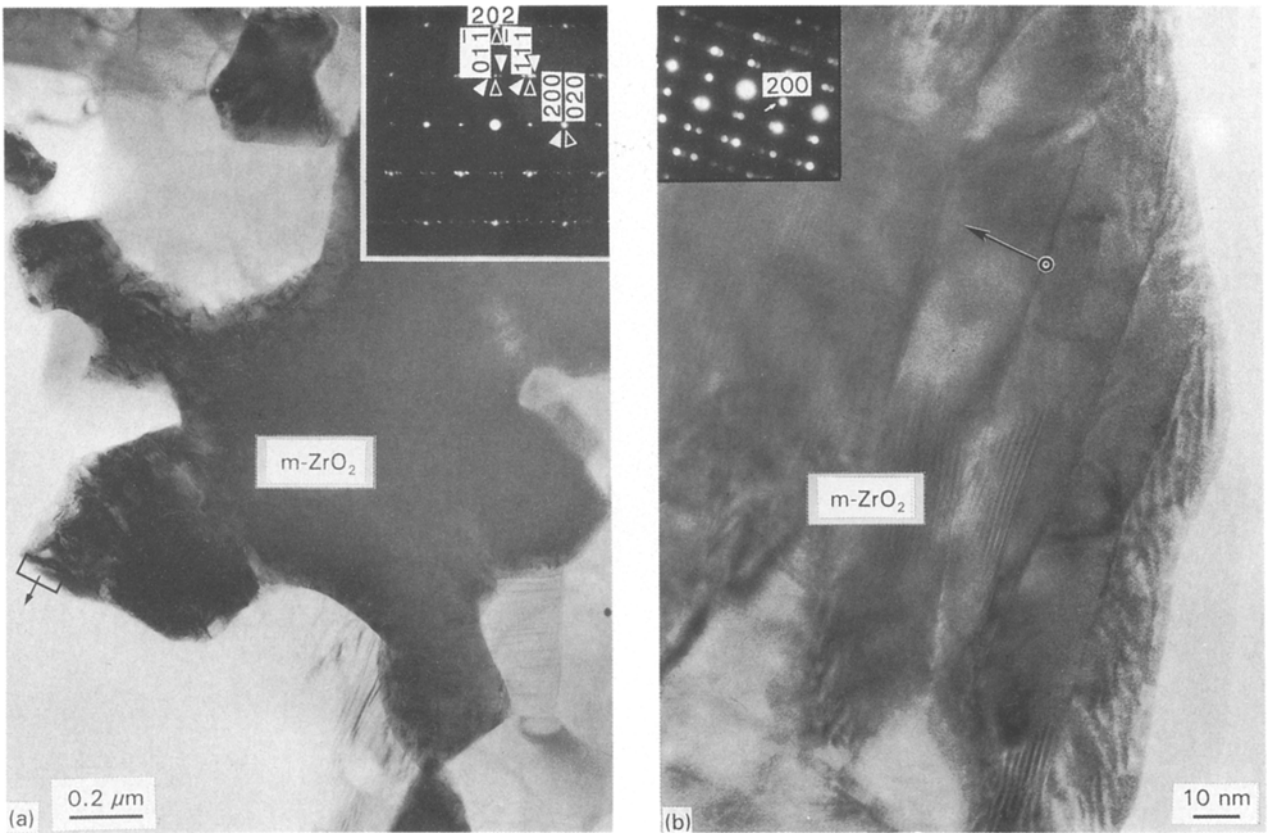

Figure 4(a) TEM bright field image (300 kV) of a polycrystalline m-ZrO_2 aggregate from SRBSN–ZrO_2 microstructure equivalent to the first dilatometer maximum. For enlargement of boxed region see (b). Two different m-ZrO_2 orientations contribute to the SAD pattern (see inset) of the aggregate. Bragg spots referring to the [0 1 1] orientation are indicated by solid triangle symbols, those resulting from the [$\bar{1}$ 0 1] orientation by open triangles, respectively. Due to twinning on {1 0 0} planes the [0 1 1] pattern gives rise to the formation of twin spots for e.g. (0 1 $\bar{1}$) and (1 1 $\bar{1}$) reflections. Note splitting of higher-order Bragg spots along a* in the [0 1 1] orientation, which separates the {h 0 0} spots from the {0 h 0} spots of the [$\bar{1}$ 0 1] diffraction pattern. (b) TEM micrograph (300 kV) displaying the {1 0 0} twin structure of the m-ZrO_2 aggregate from (a) close to the edge of the TEM-foil. The CBED pattern was taken from the twin boundary (see dot symbol) and refers to a [0 1 1] orientation parallel to the electron beam.

morph. The resulting microstructure of a 10 mol % ZrN–ZrO_2 batch consists of m-ZrO_2 precipitates embedded in a c-ZrO_2 matrix [31]. Concerning suitable Zr-oxynitrides, a detailed TEM inspection of the ZrO_2–(5-25 mol %) ZrN system [29, 30] revealed the formation of a rhombohderal $Zr_7O_{11}N_2$ phase (see Table II), which is closely related to c-ZrO_2. Its symmetry, however, is reduced because of the vacancies introduced by the substitution of nitrogen for oxygen. Upon quenching from approximately 1900 °C, the rhombohedral matrix is stabilized by small (0.3 μm) monoclinic and (to a minor extent) tetragonal precipitates.

Thus for either case the resulting microstructure of a "cubic"-ZrO_2 matrix containing monoclinic and/or tetragonal precipitates defines a characteristic feature which, however, as discussed above, was not observed for the SRBSN–ZrO_2 microstructures. CBED patterns (in particular the evaluation of FOLZ-ring radii), collected from small regions of the Zr-bearing secondary phases, did not match the matrices of either c-, t-ZrO_2, nor the rhombohedral $Zr_7O_{11}N_2$ phase or any other Zr-oxynitride from Table II. Apart from Zr and oxygen, small-probe microanalysis (EDS) only recorded a small but remarkably constant amount of Si from the Zr-bearing secondary-phase regions (see Section 3.2). Identification of nitrogen, as expected in the case of the $Zr_7O_{11}N_2$ phase, could have failed because of (i) a minimum detection limit of approximately 5 at % nitrogen with the ultra-thin window Ge-detector system employed, and (ii) experimental constraints involving the deconvolution of EDS spectra from low Z-elements, as oxygen is present in the zirconia structure and carbon was used as coating material.

It is interesting to compare the compositions of the Zr-bearing secondary phases in the SRBSN materials from this study with those reported for HIPed or pressureless sintered Si_3N_4–ZrO_2 materials of similar composition, which mostly correspond to SRBSN microstructures of the first densification event. Based on X-ray data, Lange *et al.* [34] reported c-ZrO_2 for a Si_3N_4–20 vol % ZrO_2 material, but could not confirm the $Zr_7O_{11}N_2$ phase in the presence of Si_2N_2O. Falk *et al.* [35] list the presence of possible c-ZrO_2 and t-ZrO_2 for batches employing unstabilized zirconia. It is believed that the discrepancies between the different Si_3N_4 materials are related to the densification process of the SRBSN material, which will be discussed in Section 3.2 in more detail.

According to thermodynamic calculations in the ZrO_2–ZrN system [33, 36], Zr-oxynitride phases decompose irreversibly to m-ZrO_2, ZrN and nitrogen at temperatures above 1200 °C, starting at as low as 500 °C [37]. These results are consistent with the

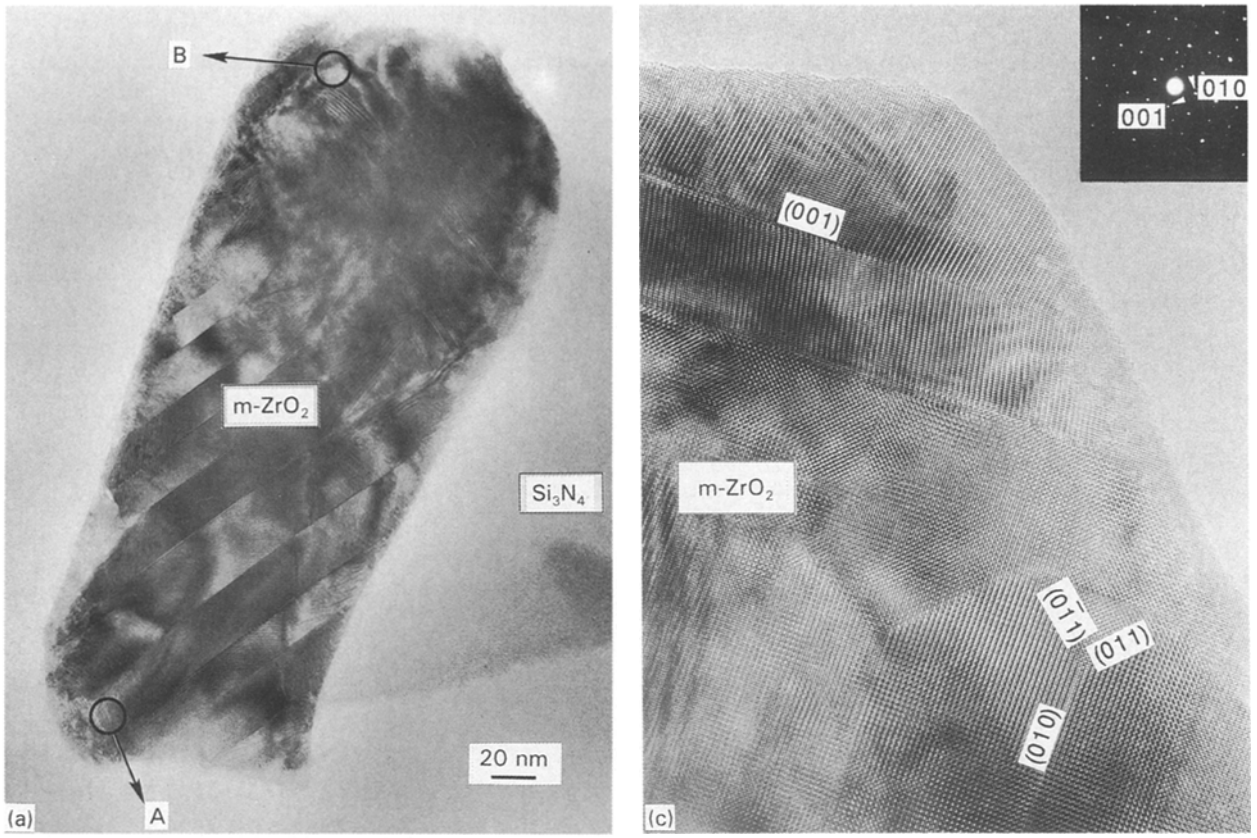

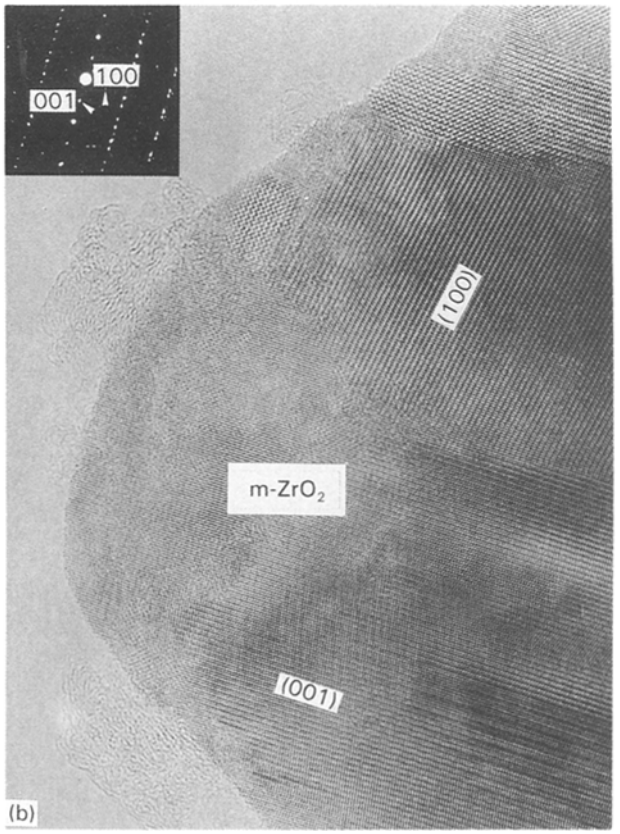

Figure 5(a) TEM micrograph (300 kV) of lath-shaped, m-ZrO_2 crystal with complex internal twinning, taken from SRBSN–ZrO_2 microstructure equivalent to the first dilatometer maximum. (b) HREM image (400 kV) from region A. The orientation is parallel to [010] revealing (001) twins, see SAD pattern inserted. (c) HREM image (400 kV) from region B. The orientation of this part of the crystal is parallel to [100] revealing different twin sections along (001) and {011} boundaries. (The SAD aperture also included some weak reflections from the β-Si_3N_4 matrix adjacent to the m-ZrO_2 particle).

TEM observations, revealing that m-ZrO_2 is the prominent secondary phase in this SRBSN material (first dilatometer maximum). ZrN was only present as a thin golden coating on the specimen surface, but could not be detected in the bulk material. During sintering, Si_3N_4 could react with ZrO_2 on the specimen surface to form ZrN according to [33, 36]

$$4\,Si_3N_4 + 6\,ZrO_2 \Rightarrow 12\,SiO(g) + 6\,ZrN + 5\,N_2(g) \quad (1)$$

ZrN is only found as a thin coating on the specimen surface, because the gaseous constituents in this reaction can escape from the system. Moreover, above 1400 °C the following reactions can take place, retransforming ZrN back to ZrO_2

$$2\,SiO_2 + ZrN \Rightarrow ZrO_2 + 2\,SiO(g) + 0.5\,N_2(g) \quad (2)$$

$$3\,SiO_2 + 2\,ZrN \Rightarrow Si_2N_2O + 2\,ZrO_2 + SiO(g) \quad (3)$$

Therefore it is very unlikely that ZrN is dispersed throughout the bulk. As mentioned earlier, X-ray data in addition to CBED revealed m-ZrO_2 as the only Zr-containing phase in this material.

Apart from the Zr-containing secondary phases, Si_2N_2O was observed in the material corresponding to the first low-temperature sintering event. Although with respect to its thermal stability, Si_2N_2O is a transient secondary phase in the Si_3N_4–ZrO_2 system, it plays an important role during liquid-phase sintering of Si_3N_4 ceramics. This becomes evident on comparing the characteristic microstructural features

TABLE II Symmetry, lattice parameters (nm) and corresponding references for the Zr-oxynitride-phases $ZrO_{2-2x}N_{4x/3}\square_{2x/3}$ described in the ZrO_2 – ZrN system

Zr–O–N phase	Symmetry	Lattice parameters (nm)	References
γ–$Zr_2ON_2\square_1$	Cubic	a = 1.0135	[29] [30] [32]
β–$Zr_7O_8N_4\square_2$	Rhombohedral	a = 0.9540 c = 0.8834	[29] [30] [32]
β'–$Zr_7O_{11}N_2\square_1$	Rhombohedral	a = 0.9560 c = 1.7600	[27] [28] [29] [30] [32]

□ Vacancy in the oxygen sublattice.

of Si_2N_2O microcrystals from the Si_3N_4–ZrO_2 material with other liquid-phase sintered Si_3N_4-based materials, e.g. the SiO_2–Si_3N_4 binary system [38]. Si_2N_2O grains develop a characteristic prismatic habitus parallel to [0 1 0] with a remarkable high density of planar faults parallel to (1 0 0) (see Fig. 6). They contain numerous small spherical intragranular inclusions, which were identified as α-Si_3N_4 by means of HREM and CBED (Fig. 7). This appearance matches recent observations obtained from Si_2N_2O microcrystals formed during liquid-phase sintering in the system SiO_2–Si_3N_4 [39, 40]. Although Si_2N_2O precipitates in general could be formed by a reaction process involving reaction 3, these results suggest that the formation of Si_2N_2O is independent of the nature of the sintering aid involved in the liquid-phase formation. This argument is supported by the fact that

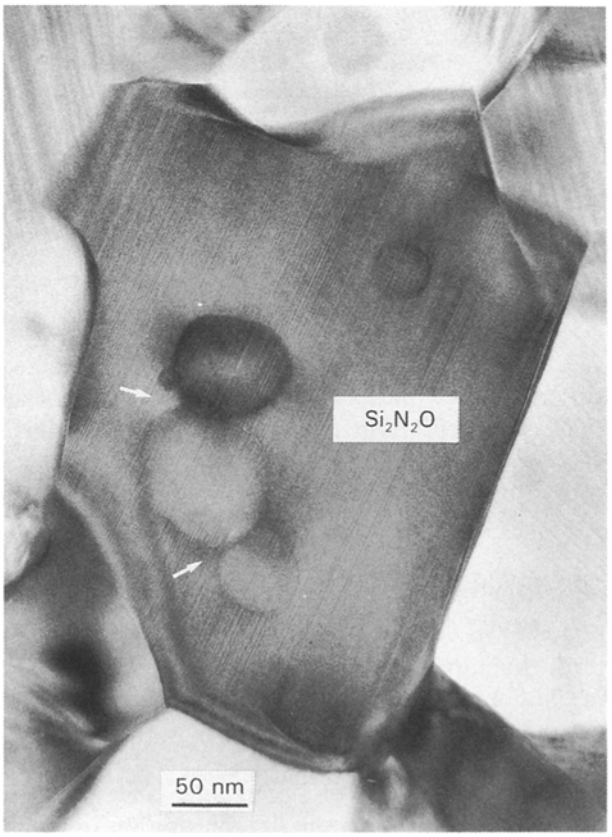

Figure 6 Si_2N_2O crystal (TEM, BF) with intergranular spherical inclusions (see arrows), identified as α-Si_3N_4. The image is taken from SRBSN–ZrO_2 microstructure equivalent to the first dilatometer maximum. Note the high density of planar defects in the Si_2N_2O grain.

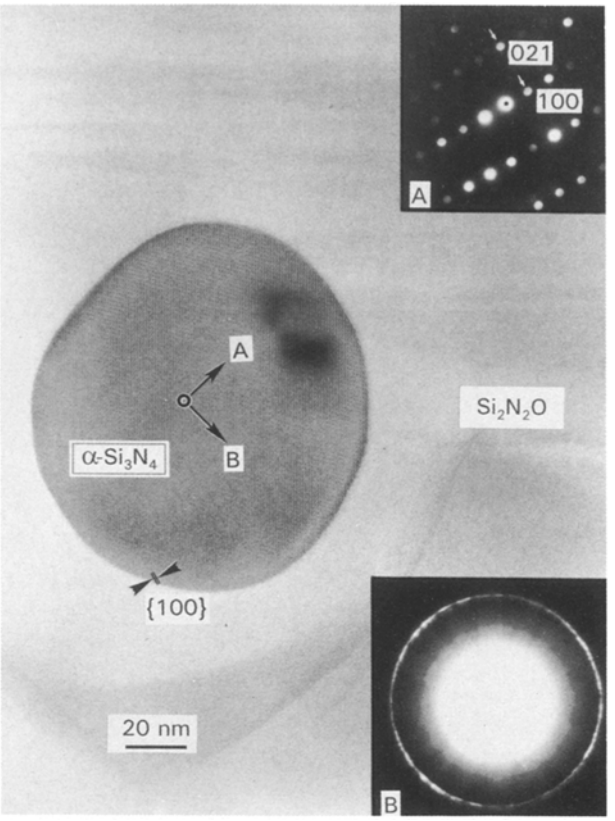

Figure 7 HREM image (300 kV) of spherical α-Si_3N_4 particle bound intergranularly to Si_2N_2O host crystal. Orientation of the particle (see CBED pattern inserted) is parallel to [0$\bar{1}$2] revealing {1 0 0} lattice fringes.

Si_2N_2O microcrystals are not restricted to reaction zones adjacent to ZrO_2 particles and that small intragranular α-Si_3N_4 inclusions are always present in Si_2N_2O grains. Therefore, the following reaction scheme is proposed

$$SiO_2 + \beta\text{–}Si_3N_4 + \alpha\text{–}Si_3N_4 \Rightarrow 2\,Si_2N_2O + (\alpha\text{–}Si_3N_{4(\text{nuclei})}) \quad (4)$$

which is in agreement with the type of reactions reported in the literature [41, 42] and investigations on the kinetics of Si_2N_2O formation in the system SiO_2–Si_3N_4 (+ 3 mol % Al_2O_3) performed by Huang *et al.* [38]. Here the formation of Si_2N_2O started at 1500 °C. The keypoint regarding the role of α-Si_3N_4 particles during the formation of Si_2N_2O is that they may act as nucleation sites during growth of Si_2N_2O in SiO_2 containing Si_3N_4 materials [40]. However, in the ZrO_2-fluxed SRBSN materials, eutectic SiO_2-rich liquid is formed at approximately 1680 °C (as

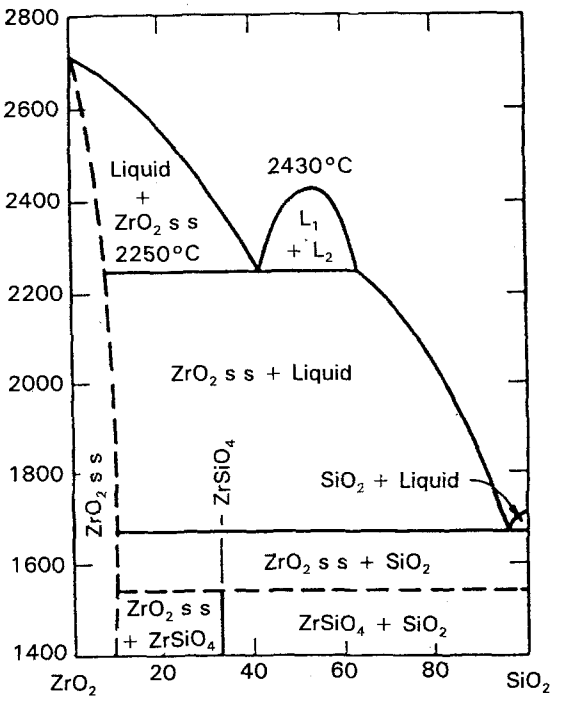

Figure 8 The system ZrO_2–SiO_2 under normal pressure emphasizing the coexistence of a silica-rich liquid phase and ZrO_2 at temperatures exceeding 1775 °C and the small solubility of SiO_2 in ZrO_2, after [50]. ss = solid solution.

deduced from the ZrO_2–SiO_2 binary; see Fig. 8) and, as the α/β Si_3N_4 phase transformation is not yet completed at this temperature, Si_2N_2O is formed surrounding the α-Si_3N_4 particles, which is in accordance with calculated phase relationships in the ZrO_2–Si_3N_4 system reported by Gauckler *et al.* [37]. It is important to note that Si_2N_2O is a transient phase in this temperature range of 1700–1800 °C, and will decompose at higher sintering temperatures (see Section 3.2) influencing the densification behavior of the material. Hence, the relatively low densification rate of the first dilatometer maximum of 5 $\mu m\,min^{-1}$ can be related to the formation of a SiO_2-rich eutectic liquid enhancing particle rearrangement. Moreover, the results suggest that the formation of Si_2N_2O grains during the first dilatometer event influences further densification as the SiO_2 content in the liquid phase present at elevated temperatures is changed. With increasing sintering temperature and duration of the experiment, the SiO_2 content and hence the amount of liquid is lowered by the Si_2N_2O formation retarding further densification. This is consistent with the dilatometer measurements shown in Fig. 2.

3.2. Microstructure of ZrO_2-fluxed SRBSN corresponding to the second dilatometer maximum

Unexpectedly, the SRBSN grades could be fully densified during post-sintering with as little as 5 wt % zirconia and no other sintering additions. The overall microstructure of the dense bodies is characterized by large elongated β-Si_3N_4 grains embedded in a fine-grained β-Si_3N_4 matrix. The crystalline secondary phase located at triple-grain junctions is homogeneously distributed throughout the bulk (Fig. 9).

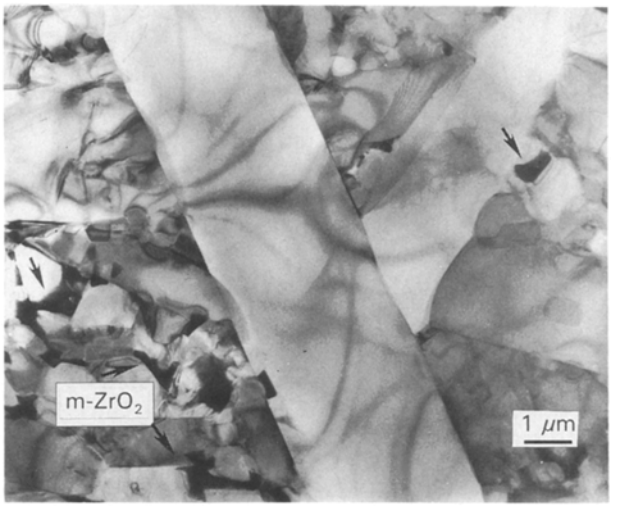

Figure 9 TEM bright field image of fully densified SRBSN–ZrO_2 material (equivalent to second dilatometer maximum) showing large elongated β-Si_3N_4 grains embedded in a fine-grained β-Si_3N_4 matrix. The secondary phase (m-ZrO_2) is homogeneously distributed at triple-grain junctions. No large secondary phase agglomerates are observed.

Compared to the first dilatometer event, both densification behaviour and microstructural development of the ZrO_2-fluxed SRBSN changed drastically under the conditions of the second dilatometer maximum. As emphasized above, the material was fully densified and no large secondary-phase agglomerates were observed (compare Fig. 3). This indicates that ZrO_2 is actively involved in the liquid-phase formation process. In this system, ZrO_2 presumably acts as an effective sintering aid because of the increased sintering temperatures and the high N_2-overpressure during the second dilatometer event, which promotes active participation of ZrO_2 in the liquid formation. As mentioned above, Si_2N_2O is no longer present in the microstructure. Huang *et al.* [38] reported on the thermal degradation of Si_2N_2O above 1830 °C releasing additional SiO_2 and Si_3N_4 and therefore increasing the liquid-phase amount in the Si_3N_4–ZrO_2 system. Hence both Si_2N_2O and ZrO_2 participate in the liquid-phase formation and give rise to the strongly pronounced densification rate of 70 $\mu m\,min^{-1}$ observed in the second dilatometer maximum. Further evidence for the active participation of m-ZrO_2 with the liquid-phase formation process also stems from the small, but remarkably constant silicon solubility in the m-ZrO_2 (approximately 2–3 wt %), which was established for all of the secondary-phase particles investigated. A typical EDS spectrum of one of the m-ZrO_2 precipitates is shown in Fig. 10. This result may be rationalized in terms of the ZrO_2–SiO_2 phase diagram (see Fig. 8), where it is a zirconia solid solution of similar composition that defines the tie line with a silica-rich liquid phase. This finding emphasizes that the phase relationships involving zirconia are mainly controlled by the ZrO_2–SiO_2-, instead of the ZrO_2–ZrN system.

With increasing sintering temperature the large agglomerates of the sintering aid, (which were still present under the conditions of the first dilatometer

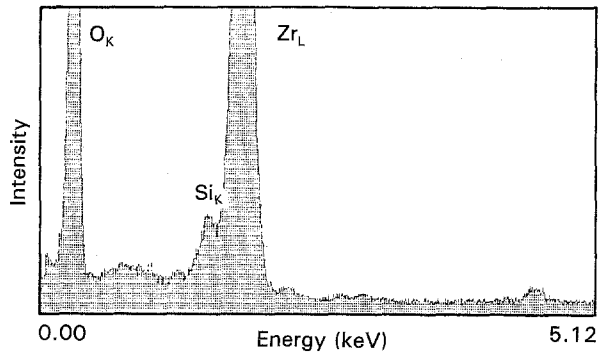

Figure 10 Typical EDS spectrum of a m-ZrO_2 particle revealing the presence of a small amount of Si apart from Zr and O; no N could be detected. It is assumed that these precipitates represent a solid solution of ZrO_2–SiO_2 ($Zr_{1-x}Si_xO_2$; compare Fig. 8).

maximum) now start to melt, thus leading to a heterogeneous distribution of liquid phase throughout the microstructure. Local solution/diffusion and reprecipitation processes of Si_3N_4 can occur, which may enhance the formation of a second generation of large elongated β-Si_3N_4 grains, as depicted in Fig. 9. Recent model experiments have shown that the formation of such elongated β-Si_3N_4 grains in Si_3N_4 materials are primarily due to the growth of pre-existing small β-Si_3N_4 grains in an α-Si_3N_4 matrix (W. Dressler, M.S. Hoffmann and E. Hampp, unpublished communication). However, due to the formation of such '*in situ*' grown elongated β-Si_3N_4 particles, an improved fracture resistance of 10 MPa $m^{1/2}$ was measured for this material [43] compared to commercial sintered silicon nitride grades of similar batch composition with an average toughness of 4–5 MPa $m^{1/2}$. The main toughening mechanisms are crack bridging and crack deflection. It is important to note that debonding along the interface of the elongated grains is a prerequisite to support these toughening mechanisms. Therefore a weak interface bonding is required, which is thought to be due to the presence of thin amorphous intergranular films generally present in Si_3N_4 materials [44–46] (compare Figs 13 and 14 below).

The crystalline secondary phase of the material, corresponding to the second dilatometer event, is homogeneously distributed at three- and four-β-Si_3N_4 grain junctions. XRD and electron diffraction confirmed only m-ZrO_2 as the apparent polymorph, with the typical internal twinned structure monitored by HREM (Fig. 11). Stabilization of m-ZrO_2 under the applied SRBSN sintering conditions may be understood by the general observation that annealing of unstabilized zirconia in pure nitrogen atmosphere will not result in the formation of the cubic polymorph [37]. The major argument against a possible formation of nitride-stabilized tetragonal or cubic polymorphs in the SRBSN system is related to the formation of an additional generation of Si_3N_4 precipitates during the second densification event. Upon cooling from the high sintering temperature, first silicon nitride will precipitate as small particles within triple-grain junctions, and/or epitaxially on facets of pre-existing Si_3N_4 matrix grains [45], leaving the residual batch composition depleted in silicon and nitrogen. Because

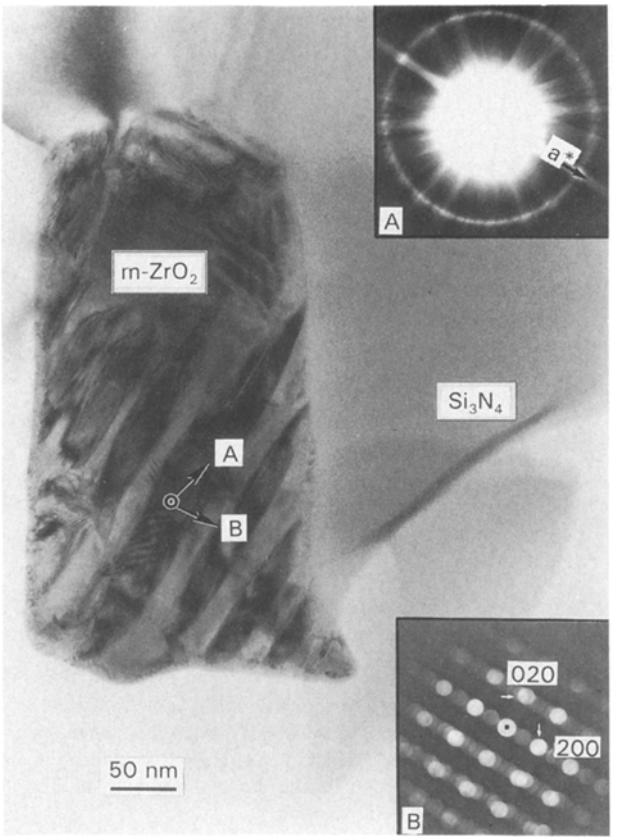

Figure 11 TEM micrograph of twinned, lath-shaped m-ZrO_2 particle, taken from fully densified SRBSN–ZrO_2 microstructure (equivalent to second dilatometer maximum). CBED patterns A and B were taken from the twin lamellae indicated by dot symbol. Beam direction is parallel to [001].

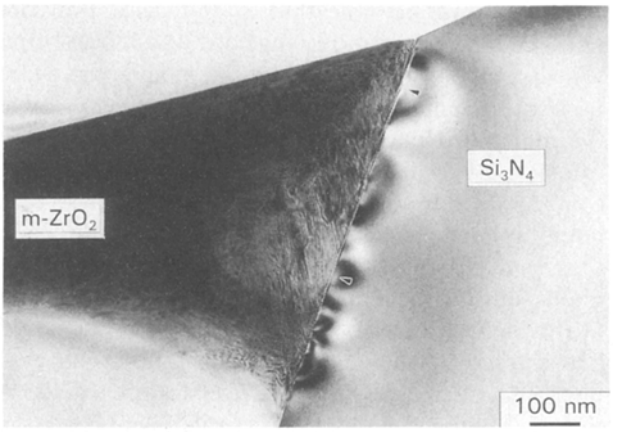

Figure 12 TEM micrograph from m-ZrO_2 particle at a triple-grain region in fully densified SRBSN–ZrO_2 material (equivalent to second dilatometer maximum). Note the strong strain contours along the m-ZrO_2/β-Si_3N_4 phase boundary.

the latter mechanisms are energetically favourable, they successfully compete for the nitrogen supplied by (i) the intrinsic high-nitrogen pressure during gas-pressure sintering and (ii) the decomposition of Si_2N_2O after the first densification event. The reduction in the overall Si_3N_4 content, either in the vapour phase or in the remaining liquid phase, is probably sufficient to prevent the stabilization of the 'cubic' zirconia at lower sintering temperatures.

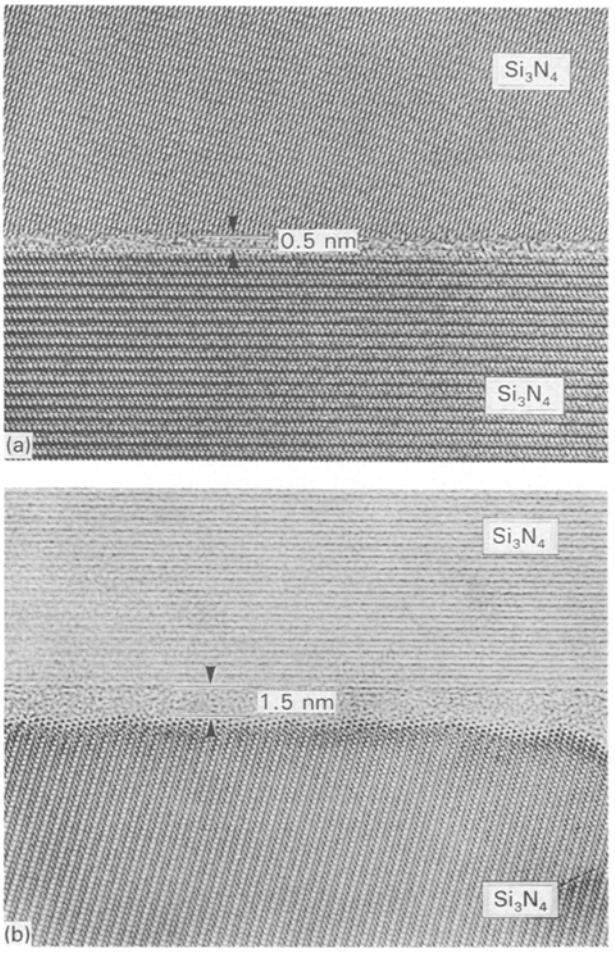

Figure 13(a) HREM image (400 kV) of β-Si_3N_4/β-Si_3N_4 grain boundary from fully densified SRBSN–ZrO_2 material (equivalent to second dilatometer maximum). The boundary is oriented edge-on with respect to the electron beam, revealing a remarkable thin amorphous layer of approximately 0.5 nm. (b) HREM image (400 kV) of β-Si_3N_4/β-Si_3N_4 grain boundary from Y_2O_3- and Al_2O_3-fluxed silicon nitride. Compare with the amorphous film width in the SRBSN + ZrO_2 material (a); a threefold increase of the layer thickness is observed.

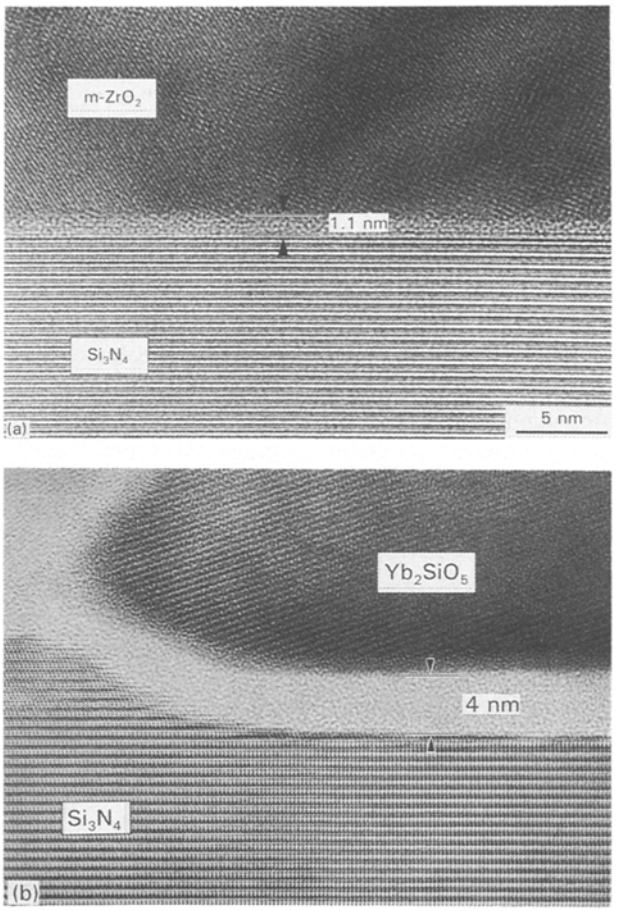

Figure 14(a) HREM image (400 kV) of m-ZrO_2/β-Si_3N_4 phase boundary from fully densified SRBSN–ZrO_2 material (equivalent to second dilatometer maximum) displaying a thickness of the amorphous interlayer of approximately 1.1 nm. Note that the phase boundary width in ZrO_2-doped SRBSN is less than the grain-boundary film thickness in Y_2O_3 + Al_2O_3-doped Si_3N_4 material (Fig. 13b). (b) HREM image (400 kV) of Yb_2SiO_5/β-Si_3N_4 phase boundary from pressureless sintered Si_3N_4 material with Yb_2O_3 addition. The amorphous film width along the phase boundary in this material is approximately 4.0 nm (compare a). Note the large difference in film thickness of both grain- and phase boundaries between the ZrO_2-doped SRBSN and other rare-earth oxide containing samples (Figs 13 and 14).

An interesting feature of this material is the presence of strong strain contours along the Si_3N_4/ZrO_2 phase boundaries (see Fig. 12). This can be due to the martensitic t ⇒ m phase transformation upon cooling with a volume increase of 3–5%. On the other hand it can be related to a characteristic microstructural feature of the dense material: HREM studies of the ZrO_2-fluxed Si_3N_4 system revealed unexpectively thin phase and grain-boundary films. The film thickness is up to three times less than in yttria and other rare-earth doped, sintered silicon nitride systems (compare Figs. 13 and 14). Additional small-probe microanalysis with a probe size of approximately 0.8 nm (using a dedicated STEM) revealed excess O, but no Zr could be detected in the amorphous grain-boundary film [46]. This is inconsistent with the ZrO_2–SiO_2 binary phase diagram (see Fig. 8), where a solubility of about 12 wt % ZrO_2 in the liquid is shown. However, regarding ELS and EDS analysis, using a dedicated STEM with a probe size of less than 1.0 nm, the detectability of small amounts of cations in these amorphous intergranular films is rather limited, owing to the small volume analysed and, in addition, to serious radiation damage during spectra aquisition. However, it is thought that traces of zirconium are present along the grain boundaries in the SRBSN–ZrO_2 system, but could not be detected. Moreover, the fact that all m-ZrO_2 particles analysed showed a constant Si content forming a ZrO_2–SiO_2 solid solution ($Zr_{1-x}Si_xO_2$), which is consistent with the binary phase diagram, supports this idea. Hence the formation of a SiO_2-rich and highly viscous eutectic liquid during sintering of the ZrO_2-fluxed SRBSN is expected.

Apart from the thinness of these phase and grain-boundary films, the chemical composition of the intergranular films strongly affects the softening temperature of these amorphous structures. It should be mentioned that material properties, in particular high-temperature properties, are thought to be less sensitive to grain-boundary film width than to grain-boundary

film chemistry. Such a silica-rich intergranular film probably shows a T_g of approximately 1120 °C (for pure silica) which is higher than the t ⇒ m transformation temperature of about 950 °C [47]. This indicates that residual stresses along the β-Si_3N_4/m-ZrO_2 interface, due to thermal expansion mismatch and/or volume changes during phase transformation, cannot be released via viscous flow of the amorphous phase or solution and reprecipitation of the surrounding matrix grains, two possible mechanisms which were treated theoretically by Kessler *et al.* [48].

Preliminary studies of the mechanical behaviour of this ZrO_2-fluxed SRBSN material revealed excellent high temperature behaviour, e.g. good creep behaviour (compared to yttria or magnesia-doped materials), indicating a relatively high softening temperature of the glassy phase in this system [49]. Moreover, these results emphasize the fact that the grain-boundary structure, as well as grain-boundary chemistry, has a strong influence on the mechanical high-temperature properties of the bulk material. It can be concluded that AEM and HREM investigations of grain boundaries in polycrystalline structural ceramics reveal very important characteristics which can be related to bulk material properties.

4. Conclusions

Densification behaviour of Zr-fluxed SRBSN, monitored by a modified dilatometer with improved sensitivity, was correlated to the microstructural development of the material using conventional TEM, HREM and AEM. Two distinct densification events were observed at 1730–1750 °C and 1900–1920 °C. The densification rate during the first dilatometer maximum was relatively low, with 0.5 μm min^{-1} compared to the second which was strongly pronounced, with 70 μm min^{-1}. TEM investigations of thin foils corresponding to the two dilatometer maxima showed marked differences regarding both phase composition and microstructure.

The material of the first densification event was characterized by a homogeneously fine-grained Si_3N_4 matrix with a high amount of residual porosity. Large secondary-phase agglomerates were observed, probably due to insufficient powder processing. XRD and electron diffraction revealed Si_2N_2O and m-ZrO_2 as the prominent crystalline secondary phases. No evidence was obtained for either the stabilization of c-ZrO_2 or the formation of constituents from the ZrO_2–ZrN system in all SRBSN–ZrO_2 materials investigated. The low densification rate of the first dilatometer event can be related to the formation of a silica-rich highly viscous liquid phase, promoting mainly rearrangement of the matrix grains.

The material of the second dilatometer maximum was completely densified. No large secondary phase agglomerates were observed in this material. Moreover, Si_2N_2O was no longer present, indicating that ZrO_2 and Si_2N_2O are actively involved in liquid-phase formation at this stage of sintering, which is consistent with the pronounced densification rate of the second dilatometer maximum. HREM revealed very thin phase- and grain-boundary films in this material (up to three times less compared with yttria-doped grades). Additional AEM using a dedicated STEM showed O at the grain boundaries, but no Zr could be detected. This is consistent with the ZrO_2–SiO_2 binary, revealing the formation of a silica-rich eutectic at 1680 °C. Moreover, the presence of such thin amorphous phase and grain-boundary films, characterized by a high softening temperature, are thought to be responsible for strong strain contours observed at phase boundaries. Residual stresses along the phase boundaries due to the martensitic phase transformation of ZrO_2 with a 3–5% volume increase cannot be released via viscous flow of the amorphous secondary phase or solution-precipitation processes.

It was shown that the two dilatometer maxima are unequivocally correlated with the compositional and microstructural development of the material during sintering, observed by means of HREM and AEM. Moreover, this densification process results in ZrO_2-fluxed SRBSN materials with good high-temperature performance.

Acknowledgements

The authors would like to thank Professor M. Rühle for many helpful discussions, and Dr J. Bruley for his support during the investigations using the dedicated STEM. The dedication of G. Paul, DLR, for her excellent preparation of thin TEM foils is gratefully appreciated.

References

1. K. KIJIMA and S. SHIRASAKI, *J. Chem. Phys.* **65** (1976) 2668.
2. C. D. GRESKOVICH, S. PROCHAZKA and J. H. ROSOLOWKI, in *Nitrogen Ceramics*, ed. F. L. Riley, p. 351, Nordhoff Leyden (1977).
3. S. C. SINGHAL, *Ceramurgia Int.* **2** (1976) 123.
4. W. A. SANDERS and D. M. MIESKOWSKI, *Amer. Ceram. Soc. Bull.* **64** (1985) 304.
5. E. TANI, M. NISHIJIMA, H. ICHINOSE, K. KISHI and S. UMEBAYASHI, *Yogyo-Kyokai-Shi* **94** (1986) 300.
6. W. A. SANDERS and D. M. MIESKOWSKI, *Adv. Ceram. Mater.* **1** (1986) 166.
7. S. DUTTA and B. BUZEK, *J. Amer. Ceram. Soc.* **67** (1984) 89.
8. L. K. L. FALK and G. L. DUNLOP, *J. Mater. Sci.* **22** (1987) 4369.
9. E. M. KNUTSON, L. K. L. FALK and T. EKSTRÖM, in *Euro-Ceramics 1*, ed G. de With, R. A. Terpstra and R. Metselaar, p. 416, Elsevier, London (1989).
10. L. K. L. FALK and M. HOLMSTRÖM, in *Euro-Ceramics 1*, ed G. de With, p. 373, R. A. Terpstra and R. Metselaar, Elsevier, London (1989).
11. J. R. KIM and C. H. KIM, *J. Mater. Sci.* **25** (1990) 493.
12. T. EKSTRÖM, L. K. L. FALK and E. M. KNUTSON-WEDEL, *J. Mater. Sci. Lett.* **9** (1990) 823.
13. G. G. DEELEY, J. M. HERBERT and N. C. MOORE, *Powder Met.* **8** (1961) 145.
14. R. W. RICE and W. J. McDONOUGH, *J. Amer. Ceram. Soc.* **58** (1975) 264.
15. H.-J. KLEEBE, G. WÖTTING and G. ZIEGLER, in *Proc. of the 6th CIMTEC World Congress on High Tech Ceramics*, Milan, Italy, ed by P. Vincencini, pp. 993–1002, Elsevier, Amsterdam, Netherlands, (1987).
16. A. GIACHELLO and P. POPPER, *Ceramurgia Int.* **5** (1979) 110.

17. J. A. MANGELS, *Ceram. Eng. Sci. Proc.* **2** (1981) 589.
18. H.-J. KLEEBE, G. WÖTTING and G. ZIEGLER, *Sci. Ceram.* **14** (1987) 407.
19. A. J. MOULSON, J. Mater. Sci. **14** 1017 51 (1979).
20. J. A. MANGELS, J. Mat. Sci. **15** 2132–35 (1980).
21. W. LUXEM, Patent pending (1992).
22. E. BISCHOFF and M. RÜHLE, J. Am. Ceram. Soc. **66** [2] 123 26 (1983).
23. A. H. HEUER, S. KRAUS-LANTERI, P. A. LABUN, V. LANTERI and T. E. MITCHELL, Ultramicroscopy **18** 335–48 (1985).
24. M. RÜHLE, L. T. MA, W. WUNDERLICH and A. G. EVANS, Phisica B **150** 86–98 (1988).
25. R. CHAIM, D. G. BRANDON and A. H. HEUER, Acta Met. **34** [2] 1933 39 (1986).
26. H. K. SCHMID, J. Am. Ceram. Soc. **70** [5] 367–76 (1987).
27. J. C. GILLES, Rev. Hautes Temp. Refract. **2** 237 (1965).
28. R. COLLONGUES, J. C. GILLES, A. M. LEJUS, M. PEREZ Y JORBA and D. MICHEL, Mat. Res. Bull. **2** 837–48 (1967).
29. G. VAN TENDELOO and G. THOMAS, Acta Met. **31** 1611–18 (1983).
30. G. VAN TENDELOO, L. ANDERS and G. THOMAS, Acta Met. **31** 1619–25 (1983).
31. N. CLAUSSEN, R. WAGNER, L. J. GAUCKLER and G. PETZOW, *Amer. Ceram. Soc. Bull.* **56** (1977) 301.
32. S. IKEDA, T. YAGI, N. ISHIZAWA, N. MIZUTANI and M. KATO, *J. Solid State Chem.* **73** (1988) 52.
33. J. WEISS, L. J. GAUCKLER, H. L. LUKAS and G. PETZOW, *J. Mater. Sci.* **16** (1981) 2997.
34. F. F. LANGE, L. K. L. FALK and B. I. DAVIS, *J. Mater. Res.* **2** (1987) 66.
35. L. K. L. FALK, T. HERMANSSON and K. RUNDGREN, *J. Mater. Sci. Lett.* **8** (1989) 1032.
36. J. WEISS, *PhD Thesis*, Stuttgart (1980).
37. L. J. GAUCKLER, J. WEISS and G. PETZOW, in *Proc. of 4th Int. Meeting on Modern Ceramics Technologies, Saint Vincent, Italy, edited by P. Vincenzini*, pp. 671–79, Elsevier Sci. Publ. Co. (1980).
38. Z. K. HUANG, P. GREIL and G. PETZOW, *Ceram. Int.* **10** (1984) 14.
39. W. BRAUE, *Mat.-wiss. u. Werkstofftech.* **21** (1990) 72.
40. W. BRAUE, R. PLEGER and R. W. CARPENTER, *J. Mater. Res.* (submitted).
41. I. SEKERCIOGLU and R. R. WILLS, *J. Amer. Ceram. Soc.* **62** (1979) 590.
42. M. E. WASHBURN, *Bull. Amer. Ceram. Soc.* **46** (1967) 667.
43. H.-J. KLEEBE and A. G. EVANS, *J. Amer. Ceram. Soc. (submitted)*.
44. H.-J. KLEEBE, N. CORBIN, C. WILLKENS and M. RÜHLE, *Mater. Res. Soc. Symp. Proc.* **170** (1990) 79.
45. J. S. VETRANO, H.-J. KLEEBE, E. HAMPP, M. J. HOFFMANN, M. RÜHLE and R. M. CANNON, *J. Mater. Sci.* **28** (1993) 3529.
46. H.-J. KLEEBE, J. S. VETRANO, J. BRULEY and M. RÜHLE, in *Proc. of 49th Annual EMSA Meeting*, August 4-9, San Jose, CA, Ed. G. W. Bailey, pp. 930–31, San Francisco Press, (1991).
47. M. RÜHLE and W. M. KRIVEN, *Ber. Bunsenges. Phys. Chem.* **87** (1983) 222.
48. H. KEßLER, H.-J. KLEEBE, R. W. CANNON and W. POMPE, *Acta Metall. Mater.* **40** (1992) 2233.
49. J. GÖRING, W. BRAUE and H.-J. KLEEBE, Key Engineering Materials, 89–91 (1994), 641, Trans Tech Publications, Switzerland.
50. *Phase Diagrams for Ceramists*, eds. E. M. Levin, C. R. Robbin, H. F. McMurdie and M. K. Reser, 3rd Edition, Fig. 362, Am. Ceram. Soc., Columbus, OH (1974).

Received 6 *October* 1992
and accepted 15 *September* 1993